Nanoscale

Accepted Manuscript

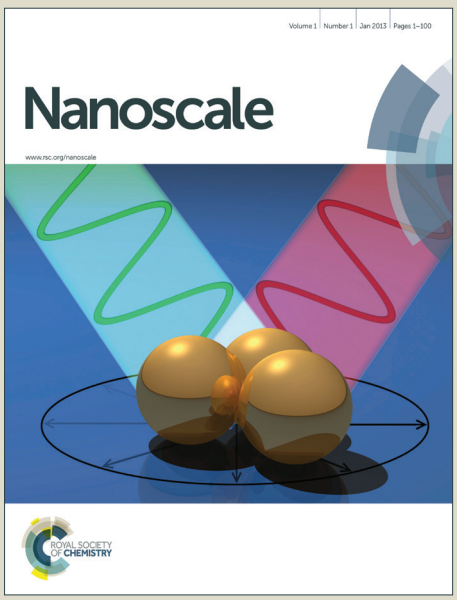

ROYAL SOCIETY OF CHEMISTRY

www.rsc.org/nanoscale

New insights on the organic-inorganic hybrid perovskite $CH_3NH_3PbI_3$ nanoparticles. Experimental and theoretical study of doping in Pb^{2+} sites with Sn^{2+}, Sr^{2+}, Cd^{2+} and Ca^{2+}

Javier Navas,* Antonio Sánchez-Coronilla,[1],* Juan Jesús Gallardo, Norge Cruz Hernández,[2] Jose Carlos Piñero,[3] Rodrigo Alcántara, Concha Fernández-Lorenzo, Desireé M. De los Santos, Teresa Aguilar, Joaquín Martín-Calleja

Departamento de Química Física, Facultad de Ciencias, Universidad de Cádiz, E-11510 Puerto Real (Cádiz), Spain; [1] Departamento de Química Física, Facultad de Farmacia, Universidad de Sevilla, 41012 Sevilla, Spain; [2]Departamento de Física Aplicada I, Escuela Técnica Superior de Ingeniería Informática, av. Reina Mercedes, Universidad de Sevilla, 41012 Sevilla, Spain, and [3]Departamento de Ciencias de los Materiales e Ingeniería Metalúrgica y Química Inorgánica, Facultad de Ciencias, Universidad de Cádiz, E-11510 Puerto Real (Cádiz), Spain.

Corresponding Authors:

*Javier Navas (javier.navas@uca.es); Antonio Sánchez-Coronilla (antsancor@us.es).

Table of Contents entry

This paper studies from an experimental and theoretical perspective the organic-inorganic hybrid perovskite, $CH_3NH_3PbI_3$, doped in Pb^{2+} position with Sn^{2+}, Sr^{2+}, Cd^{2+} and Ca^{2+}.

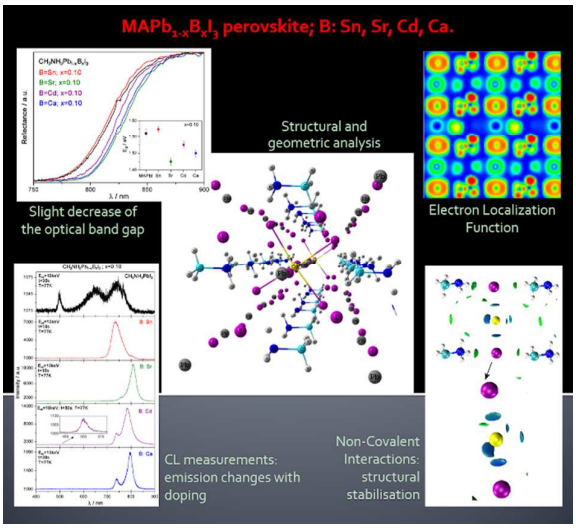

Abstract

This paper presents the synthesis of organic-inorganic hybrid perovskite, $CH_3NH_3PbI_3$, doped in Pb^{2+} position with Sn^{2+}, Sr^{2+}, Cd^{2+} and Ca^{2+}. The incorporation of the dopants into the crystalline structure was analysed, observing how the characteristics of the dopant affected properties such as the crystalline phase, emission and optical properties. XRD showed how doping with Sn^{2+}, Sr^{2+} and Cd^{2+} did not modify the normal tetragonal phase. When doping with Ca^{2+}, cubic phase was obtained. Moreover, DR-UV-Vis spectroscopy showed how the band gap decreased with the dopants, the values following the trend $Sr^{2+}<Cd^{2+}<Ca^{2+}<CH_3NH_3PbI_3\approx Sn^{2+}$. The biggest decrease was generated by Sr^{2+}, which reduced the $CH_3NH_3PbI_3$ value by 4.5%. In turn, Cathodoluminescence (CL) measurements confirmed the band gap obtained. Periodic-DFT calculations were performed to understand the experimental structures. The DOS analysis confirmed the experimental results obtained using UV-Vis spectroscopy, the values calculated following the trend $Sn^{2+}\approx Pb^{2+}>Cd^{2+}>Sr^{2+}$ for the tetragonal structure and $Pb^{2+}>Ca^{2+}$ for the cubic phase. The Electron Localization Function (ELF) analysis showed similar electron localization for undoped and Sn^{2+}-doped tetragonal structures, which was different to those doped with Sr^{2+} and Cd^{2+}. Furthermore, when Cd^{2+} was incorporated, the Cd-I interaction was strengthened. For Ca^{2+} doping, the Ca-I interaction had a greater ionic nature than Cd-I. Finally, an analysis based on the non-covalent interaction (NCI) index is presented to determine the weak-type interactions of the CH_3NH_3 groups with the dopant and the I atoms. To our knowledge, this kind of analysis with these hybrid systems has not been performed previously.

1. Introduction

Organic-inorganic hybrid perovskite is being widely studied nowadays as it has a variety of interesting optical, magnetic and electronic applications.[1-3] Specifically, perovskites based on methylammonium lead halide ($MAPbI_3$, where $MA=CH_3NH_3$) are being studied after causing a revolution in the world of photovoltaic energy due to its high efficiency up to 15%.[4-6] Electronic absorption spectra for this kind of perovskite shift to a longer wavelength, and this is one of the reasons for its high performance.[5] In turn, from a structural perspective, the reported X-ray diffraction patterns for this system have been interpreted as a tetragonal structure.[7, 8] Thus, their increased photonic absorption towards the infrared region and their crystalline structure are two vital factors in the performance of this kind of compounds. The substitution of some elements of $MAPbI_3$ with dopants to control the band gap and electronic properties has been studied from both an experimental and theoretical point of view, for example the controlled substitution of I^- with Cl^- or Br^-,[4, 7, 9-13] or Pb^{2+} with Sn^{2+}.[5, 6, 14, 15]

In this paper, we synthesized $CH_3NH_3Pb_{1-x}B_xI_3$ species, where B were Sn^{2+}, Sr^{2+}, Cd^{2+} and Ca^{2+} ions and x=0.05, 0.10, 0.15. To our knowledge, the doping of $MAPbI_3$ with Sr^{2+}, Cd^{2+} and Ca^{2+} has not been reported previously. Thus, the effect of this doping on the band gap and crystalline phase of perovskite was analysed. To do this, synthesized samples were characterized using elemental analysis techniques such as the CHNS technique or X-ray fluorescence (XRF) to corroborate the levels of dopant introduced; x-ray diffraction (XRD) determined the crystalline phases present in the samples; X-ray photon spectroscopy (XPS) determined the chemical bonding states; UV-Vis spectroscopy in diffuse reflectance mode (DR-UV-Vis) was used to establish the band gap of the samples; scanning electron microscopy (SEM) was used to observe the morphology of the nanoparticles obtained; and the cathodoluminescence (CL) technique

to analyse the optical emission of the samples. In addition, from a theoretical perspective, periodic density functional theory (DFT-periodic) calculations were performed to rationalize the experimental information on this topic. The structures $(MA)_8Pb_7SnI_{24}$, $(MA)_8Pb_7SrI_{24}$, $(MA)_8Pb_7CdI_{24}$ and $(MA)_8Pb_7CaI_{24}$ were optimized to simulate the experimental stoichiometries (with x=0.10). Density of state (DOS) results agreed with the experimental ones, showing a slight decrease in band gap energy. Moreover, the analysis of both the electron localization function (ELF)[16-20] and the non-covalent interaction (NCI)[21] shed light on the bonding interactions established within these hybrid systems. An NCI analysis with these hybrid systems has not been reported before, to our knowledge.

2. Results and Discussion

2.1. Elemental analysis

The elemental analysis of the synthesized samples (see experimental section) was performed using XRF to determine the amount of I, Pb and the dopant incorporated into the structure, and with the CHNS technique to ascertain the amount of C, H and N. The weight percentages of each of the elements in the synthesized samples were obtained (see Table S1) and the atomic percentages were determined and are shown in Table 1. From these data, only small deviations were found in x compared with the nominal composition.

2.2. X-Ray Diffraction

The XRD patterns for the undoped sample, $MAPbI_3$, and for the samples doped with x=0.10 are shown in Figure 1. The diffractograms of the rest of the samples synthesized are shown in Figure S1 in the Electronic Supplementary Information (ESI). The pattern

for $MAPbI_3$ showed several diffraction peaks, which can be indexed to planes of the tetragonal I4/mcm space, group, as reported for $MAPbI_3$ perovskite.[4, 8, 10, 11, 22, 23] The peak that corresponds with the reflection of the plane (211) of the tetragonal phase establishes the main difference with the peaks that would be observed if there were a cubic phase (Pm3m space group). But, four peaks that cannot be indexed to the tetragonal and cubic phases are observed at about 2θ = 12.8º, 26.0º, 34.2º and 39.5º. These peaks are assigned to PbI_2, used as a reagent in the synthesis. For the purpose of comparison, the pattern of the commercial PbI_2 used is shown in Figure S2A in the ESI.

Table 1. Results in atomic percentage (at.%) obtained from the elemental analysis performed using the CHNS and XRF techniques.

Sample* $MAPb_{1-x}B_xI_3$		**at.% C**	**at.% H**	**at.% N**	**at.% Pb**	**at.% I**	**at.% B**	x_{real}
$MAPbI_3$		8.4	50.0	8.4	8.3	24.9	--	0.00
B=Sn	0.05	8.3	50.1	8.3	7.9	24.9	0.5	0.05
	0.10	8.3	50.0	8.3	7.6	25.0	0.8	0.09
	0.15	8.3	50.0	8.3	7.1	25.0	1.3	0.15
B=Sr	0.05	8.3	50.0	8.3	7.9	25.0	0.5	0.05
	0.10	8.3	50.0	8.3	7.5	25.0	0.9	0.10
	0.15	8.4	49.9	8.3	7.2	25.0	1.2	0.14
B=Cd	0.05	8.3	50.1	8.3	7.9	24.9	0.5	0.05
	0.10	8.4	49.9	8.4	7.5	25.0	0.8	0.10
	0.15	8.3	50.0	8.3	7.1	25.0	1.3	0.15
B=Ca	0.05	8.4	49.9	8.3	7.9	25.0	0.5	0.06
	0.10	8.3	49.9	8.4	7.5	25.1	0.8	0.10
	0.15	8.3	50.0	8.3	7.1	25.0	1.3	0.15

*The doped samples are named according to the dopant and the nominal value of x. The real value of x is shown in the last column of the table.

The patterns with Sn^{2+} and Sr^{2+} show reflections that can be assigned to planes of the tetragonal phase with space group I4/mcm, the same as the undoped sample. In turn, PbI_2 is not present. Thus, incorporating Sn^{2+} and Sr^{2+} into the structure of $MAPbI_3$ perovskite did not affect the crystalline structure. In the patterns of the sample doped with Sr^{2+}, the peaks show a lower signal/noise ratio and are slightly wider than for

$MAPbI_3$, suggesting a slight loss of crystallinity due to the presence of the dopant. A study using a different method of synthesis reported a change from tetragonal to cubic phase due to Pb^{2+} being substituted by Sn^{2+} from values of x=0.5.[6] In our case, perovskite $MAPb_{0.5}Sn_{0.5}I_3$ was synthesized with the exclusive formation of tetragonal phase (see Figure S3 in the ESI), so attention must be paid to the methods of synthesis used to obtain this type of compound.

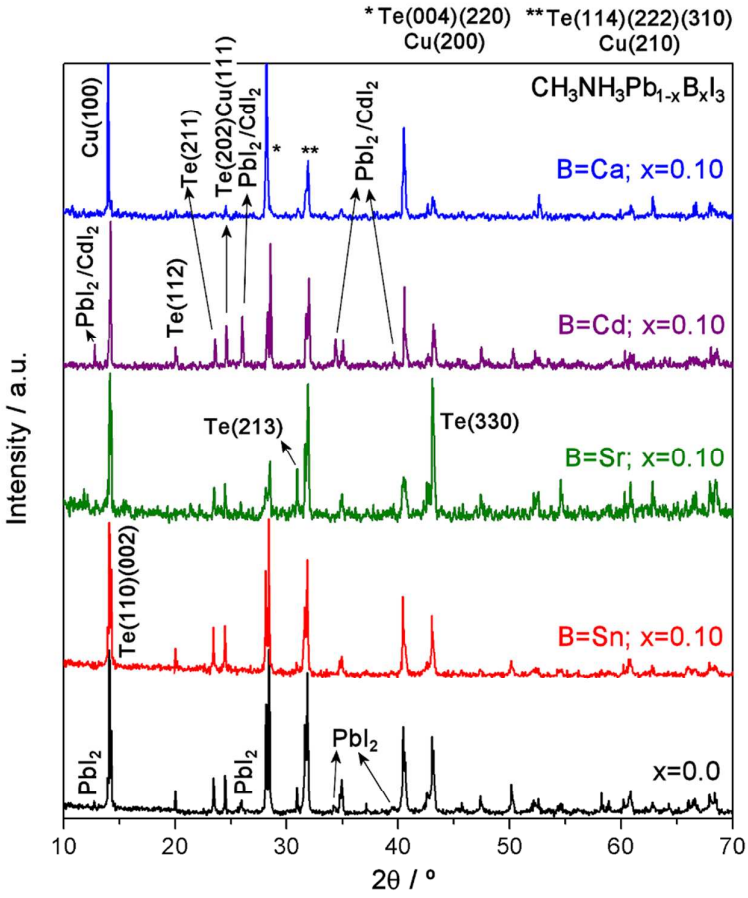

Figure 1. XRD patterns of the $MAPbI_3$ sample, and $MAPb_{1-x}B_xI_3$, with B=Sn, Sr, Cd, Ca, and x= 0.10. Te: Tetragonal phase, Cu: Cubic phase.

The patterns of the Cd-doped perovskite show the typical peaks indexed to a tetragonal I4/mcm space group. But, the patterns show the peaks assigned to PbI_2 plane

reflections, as does the undoped perovskite (see Figure 1). In this case, the intensity of the peaks is greater, possibly due to a contribution from remains of CdI_2, which also show two reflections at approximately 2θ = 12.9º, and 26º (CdI_2 pattern is shown in Figure S2B). Thus, the inclusion of Cd seems to hinder the formation reaction of perovskite.

Figures 1 and S1E in the ESI show the patterns obtained for the samples doped with Ca^{2+}. They are clearly different to those obtained for the tetragonal phase. The main peaks observed in the patterns of the Ca^{2+}-doped samples are indexed to a cubic phase of the Pm3m space group.[8] In the patterns of the undoped sample and those doped with Sn^{2+}, Sr^{2+} and Cd^{2+}, two peaks within the range 2θ = 23º-25º were observed. These peaks can be indexed to (211) and (202) planes of the tetragonal I4/mcm space group, respectively. In the pattern obtained for the sample doped with Ca^{2+}, only a single peak is observed in this range. As Baikie et al. reported, tetragonal and cubic polymorphs are readily differentiated by monitoring the peaks of the (211) and (213) reflections of the tetragonal phase (at about 2θ = 23.5º and 30.9º, respectively).[8] In turn, another peak with which the presence of tetragonal or cubic phase can be detected is the one indexed to the reflection of the plane (213) of the tetragonal I4/mcm space group, which appears at approximately 2θ = 31º. At this value of 2θ, cubic phase does not show a characteristic peak. No peak appears at this value in the patterns obtained for the samples doped with Ca^{2+}. Thus, we can confirm that in the Ca^{2+}-doped samples, cubic phase (Pm3m space group) is predominant. In turn, the presence of PbI_2 is not detected.

In conclusion, we can state that synthesized $MAPbI_3$ has a predominantly tetragonal crystalline phase (I4/mcm space group), and residues of the PbI_2 used as a reagent. The samples doped with Sn^{2+} and Sr^{2+} also have this predominant crystalline phase. The Sr^{2+}-doped sample loses crystallinity compared with the undoped perovskite, leading to

the conclusion that Sr^{2+} is incorporated into the structure of the perovskite, replacing the Pb^{2+}. As for Sn^{2+}, no significant loss of crystallinity is observed, but as will be discussed below, theoretical calculations show that its presence in Pb^{2+} positions does not lead to structural distortions in the tetragonal phase. In turn, the Cd^{2+}-doped samples show a mixture of tetragonal phase and residues of PbI_2 and CdI_2. Cd^{2+} is also introduced into the perovskite phase replacing Pb^{2+} ions, with different optical properties being observed, as will be analysed below from an experimental and theoretical perspective. Finally, the samples doped with Ca^{2+} show a predominantly cubic phase (Pm3m space group).

2.3. UV-Vis spectroscopy

Diffuse reflectance UV-Vis measurements were performed to determine the optical band gap energy (E_g). Figure 2 shows a region of the spectra obtained for the $MAPbI_3$ and $MAPb_{1-x}B_xI_3$ samples, with x=0.10. In turn, Figure S4 in the ESI shows all the spectra obtained. Figure 2 shows that the presence of Sn^{2+} leads to a slight blue-shift of the absorption band, while the presence of the other dopants leads to a red-shift, following the trend Sr^{2+}>Ca^{2+}>Cd^{2+}. Furthermore, changes in the x values hardly modify the spectra obtained.

The band gap of the samples can be determined from the UV-Vis spectra in diffuse reflectance mode. The optical absorption coefficient (α/S) is calculated using the reflectance data according to Kubelka-Munk equation,[24]

$$F(R) = \left(\alpha/S\right) = \frac{(1-R)^2}{2R}, \quad (1)$$

where R is the percentage of light reflected, and α and S are the absorption and scattering coefficients, respectively. The incident photon energy ($h\nu$) and the optical band gap (E_g) are related according to the expression

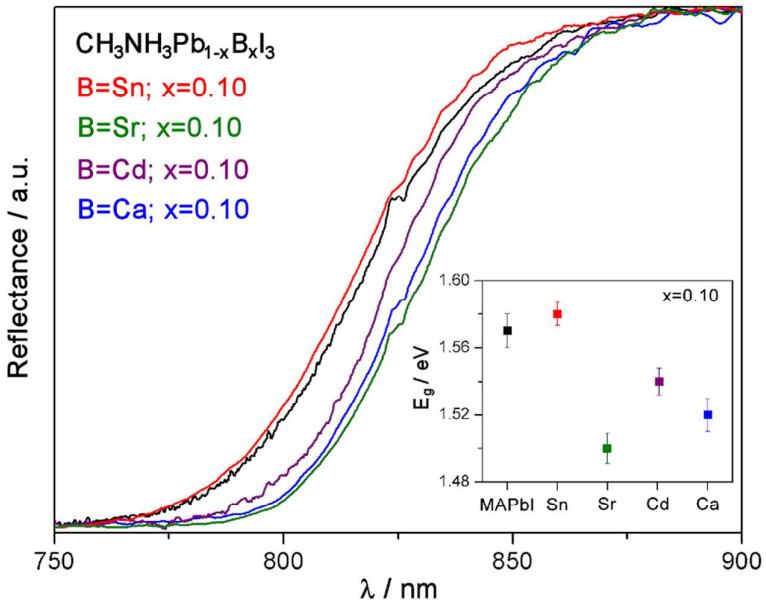

Figure 2. Diffuse reflectance UV-Vis spectra for the $MAPbI_3$ sample, and $MAPb_{1-x}B_xI_3$, with B=Sn^{2+}, Sr^{2+}, Cd^{2+}, Ca^{2+}, and x= 0.10. In the inset, the plot of the optical band gap values for each sample.

$$[F(R) \cdot h\nu]^p = A\left(h\nu - E_g\right), \qquad (2)$$

where A is a constant that depends on the transition probability and p is the power index that is related with the optical absorption process. Theoretically, p equals ½ or 2 for an indirect or a direct allowed transition, respectively.[12] According to the literature, the optical absorption for this kind of perovskite occurs via direct transition.[7] So, the optical band gap E_g was determined from the extrapolation of the linear part of the $[F(R)\cdot h\nu]^2$ vs $h\nu$ plot. The values found are shown in Table 2. They show how doping with Sn^{2+} did not affect the optical band gap, while the other three dopants produced small decreases. Doping with Sr^{2+} generated the greatest decrease in the band gap value with respect of $MAPbI_3$ value, about 4.5%. Thus, the optical band gap decreased with the dopants following the trend Sr^{2+}>Cd^{2+}>Ca^{2+}. Furthermore, changing the amount of dopant did not affect the modifications in the band gap, similar values being observed for each dopant in all the proportions synthesized (see Figure S4 in the ESI). But, the

changes due to the dopant concentration could be lesser than the resolution of the measurement methodology used, and therefore this effect could not be observed.

A sample was synthesized according to the formula $MAPb_{0.5}Sn_{0.5}I_3$, for which the literature reports optical band gap values below 1.3 eV with cubic phase.[6] Our sample showed a tetragonal phase, as has been shown before, and the optical band gap value obtained was 1.57 eV. Figure S5 in the ESI shows a comparison of the UV-Vis spectrum in diffuse reflectance mode for this sample and the $MAPbI_3$ perovskite, no differences being observed in the optical properties of the two samples. Thus, it is possible to assert that the method used to synthesize these samples is important to control both the crystalline phase and optical properties. In turn, the band gap value probably depends on the crystalline phase present, and not only on the electronic properties of the dopant used, although the dopant does affect the crystalline phase. Thus, it is possible to confirm that both the crystalline phase in the samples and their optical band gap can be modified within a narrow range with this kind of doping.

Table 2. Optical band gap values for the samples synthesized.

$MAPb_{1-x}B_xI_3$		E_g /eV	$MAPb_{1-x}B_xI_3$		E_g /eV
B	x		B	x	
--	0.00	1.57	Cd	0.05	1.54
Sn	0.05	1.57		0.10	1.54
	0.10	1.58		0.15	1.54
	0.15	1.57	Ca	0.05	1.52
Sr	0.05	1.51		0.10	1.52
	0.10	1.50		0.15	1.52
	0.15	1.51			

2.4. X-Ray Photoelectron Spectroscopy (XPS)

XPS spectra were performed to confirm the presence of the dopants in the samples, its oxidation state and chemical bonding states. The samples of $MAPbI_3$, and $MAPb_{1-x}B_xI_3$ ($B=Sn^{2+}$, Sr^{2+}, Cd^{2+}, Ca^{2+}) with x=0.10 were analysed. Figure S6 in the ESI shows the

general XPS spectra for the samples, and Figure 3A shows zones of the spectra where the presence of the dopants stands out. The spectra are shown for Sn 3d, Sr 3p and 3d, Cd 3d and Ca 2p. In the case of Sn, the binding energy (BE) of Sn $3d_{3/2}$ and Sn $3d_{5/2}$ was around 494.9 and 486.5 eV, which is the typical position and separation of spin-orbit components for Sn^{2+}.[25] Moreover, Sr 3p and Sr 3d spectra are shown in Figure 3A. Both zones overlap with C 1s and Pb 4f signals present in the sample, but the peaks indexed to Sr can be seen. The BE of Sr $3p_{1/2}$ and $3p_{3/2}$ were around 280 and 270.2 eV, in line with those in the literature for Sr^{2+}.[25] The remaining peaks in these spectra are assigned to C 1s and its satellites. In turn, the BE of Sr $3d_{3/2}$ and Sr $3d_{5/2}$ was found to be about 136.2 and 134.5 eV, in agreement with the typical separation of both components (~1.76 eV).[25] The other peaks are assigned to Pb 4f. Furthermore, the Cd 3d spectrum is shown in Figure 3A. This zone overlaps with the signal of Pb 4d. The signal for Cd $3d_{3/2}$ overlaps completely with that of Pb $4d_{5/2}$ at around 412 eV. This peak is clearly asymmetrical, denoting that it is formed by several contributions. The BE of Cd $3d_{5/2}$ was obtained at about 405.9 eV, in agreement with the literature.[25] The signal at a BE around 402 eV is indexed to N 1s. So, XPS results show the presence of the dopants in the samples synthesized.

In addition, Figure 3B shows the I $3d_{3/2}$ and I $3d_{5/2}$ spectra for all the samples. The spectra show well separated spin-orbit components, a separation of around 11.4-11.5 eV being found in all the cases, which is typical of the presence of I^-.[25] In turn, the signals for some dopants were displaced compared with that for the $MAPbI_3$ sample. The signals for I $3d_{3/2}$ and I $3d_{5/2}$ for Sn-doped perovskite coincide with those obtained for $MAPbI_3$, while in other cases there is a shift towards higher BE values, suggesting that small modifications are produced in the oxidation state of I^- after doping with Sr^{2+}, Cd^{2+} and Ca^{2+}. This is corroborated by means of theoretical calculations, as shown below. As

reported previously, the optical band gap energy of these dopants decreased slightly, suggesting that the presence of the dopants slightly modified the interaction with the ions in the network, leading to changes in the band gap and, consequently, small geometrical distortions, as will be shown below by means of theoretical calculations. In the case of the interactions between the dopants and the MA groups, slight modifications can also be observed in the chemical bonding states, for example if we analyse the signals obtained for N. Figure 3C shows the spectra of N 1s for the samples studied. The BE of N 1s was around 401.5-402.4 eV. As with the signal of I 3d, small modifications are observed depending on the dopant, there being a slight shift towards a higher BE. These slight modifications in the dopant-I and dopant-MA groups interaction will be analysed using theoretical calculations.

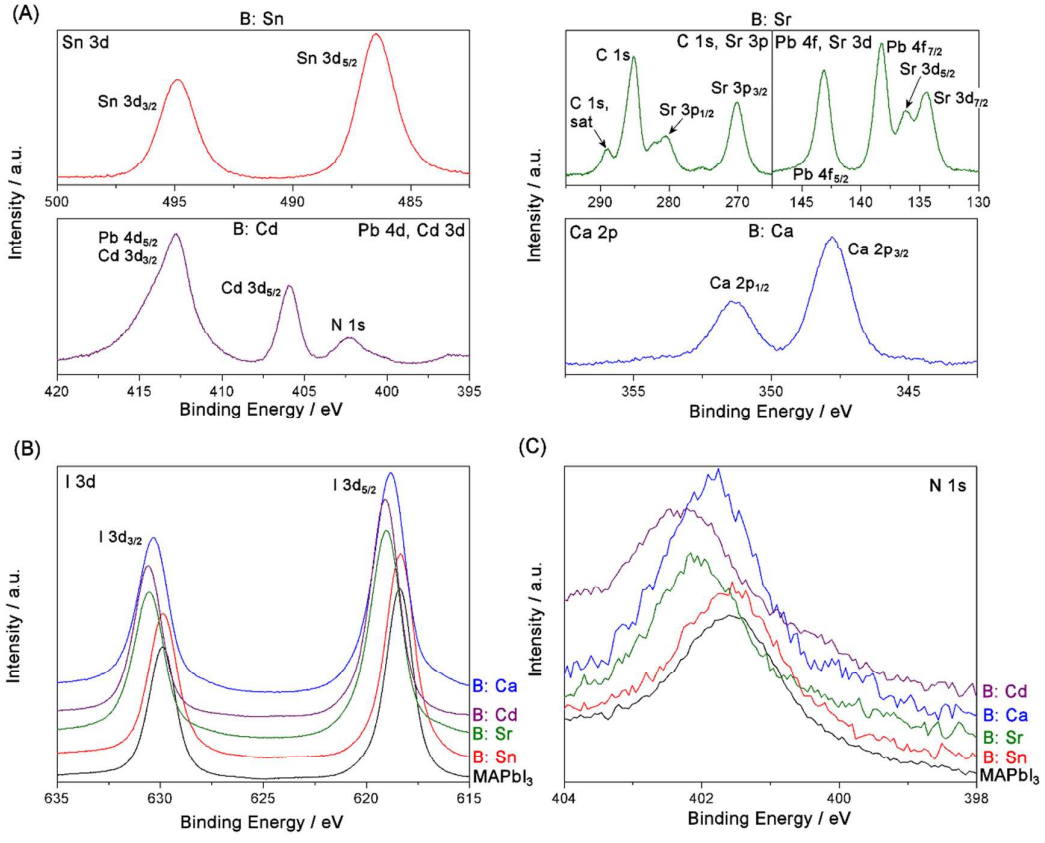

Figure 3. XPS spectra for: (A) Sn 3d, Sr 3p and 3d, Cd 3d, Ca 2p; (B) I 3d; and (C) N 1s for the samples synthesized.

2.5. SEM and Cathodoluminescence (CL)

CL spectra were performed for the undoped sample and the doped samples with x=0.10. SEM images were also obtained for these samples. Figure 4 shows representative SEM images of the samples in the zone of the CL emission under study. Different structures can be seen for the samples. The undoped and Sn^{2+}-doped samples have similar morphologies, while the other three are different. The markedly different morphology of the Ca-doped sample is of note as it is the only one with a cubic phase as the predominant crystalline phase.

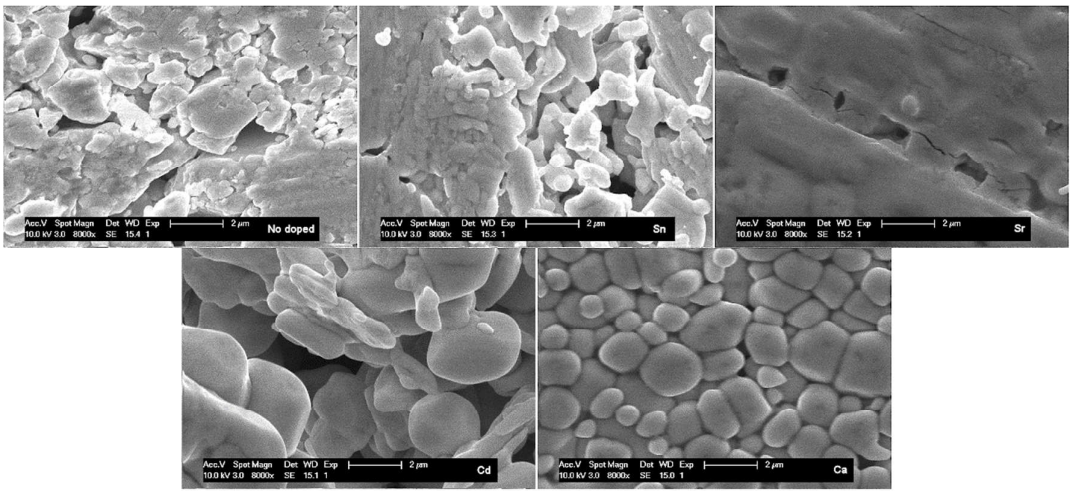

Figure 4. SEM images of the samples synthesized. x = 0.10 for all the doped samples.

Figure 5 shows the CL spectra obtained for the undoped perovskite and the samples doped with x=0.10. The first observation is that the undoped and Ca^{2+}-doped samples show lower emission values than the rest of the samples, so they will have lower recombination values. The main emission peak is around 740 nm for the undoped sample and approximately ~734, 808, 789 and 796 nm for the perovskites doped with Sn^{2+}, Sr^{2+}, Cd^{2+} and Ca^{2+}, respectively. This main emission peak coincides with the optical band gap values reported previously. The presence of other peaks is also of note.

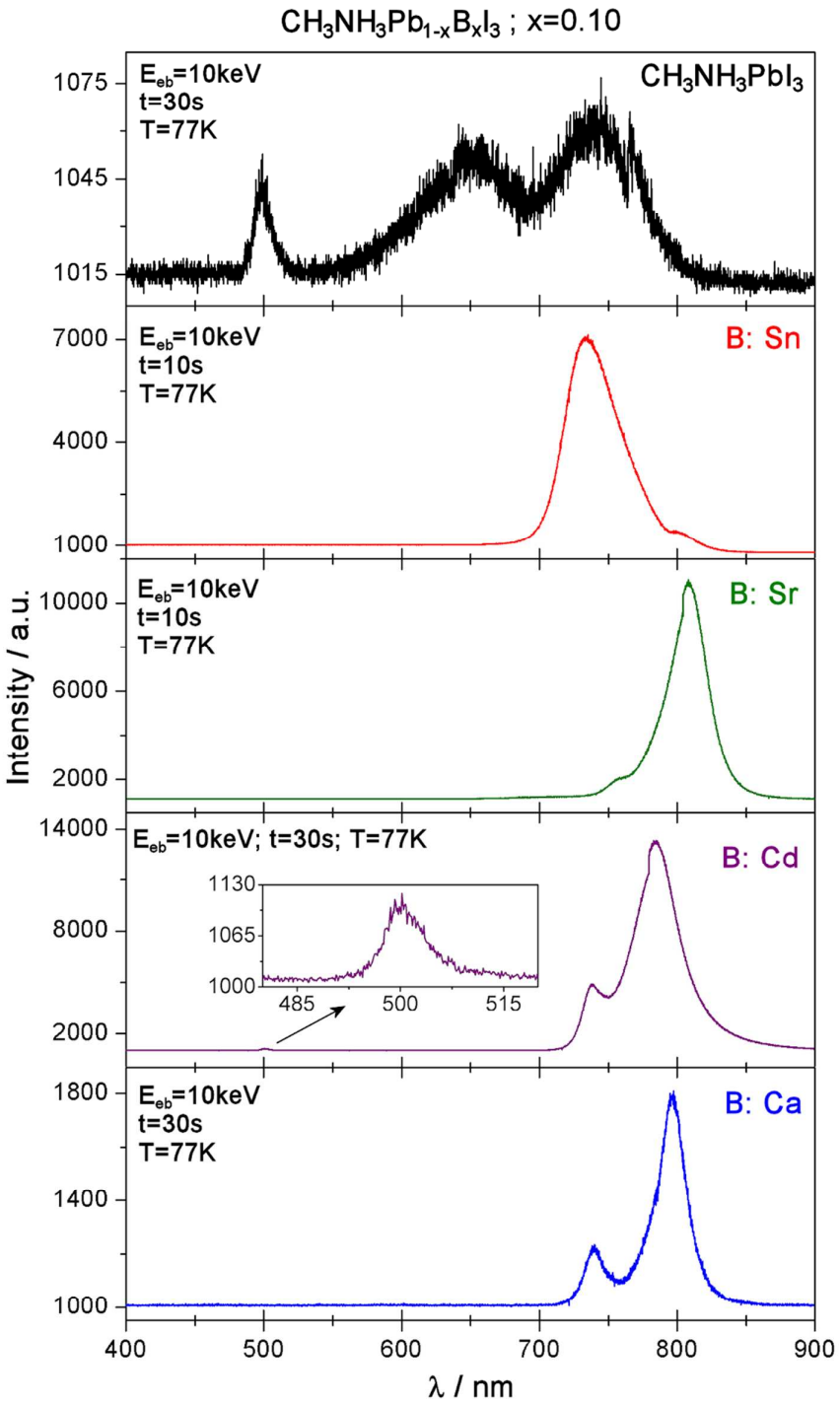

Figure 5. CL spectra of the $MAPbI_3$ sample, and $MAPb_{1-x}B_xI_3$, with B=Sn^{2+}, Sr^{2+}, Cd^{2+}, Ca^{2+}, and x= 0.10.

Apart from the main peak, there is a second emission nearby for all the doped samples, suggesting there are two different disexcitation mechanisms. The clear difference

between the sample doped with Sn^{2+} and the others suggests that the band gap is defined by which of the two is the main mechanism, the one that produces the greater emission. This is thought to depend on the kind of interactions taking place between the organic and inorganic parts of the crystal. It is important to note that these two peaks can be observed as a result of the measuring conditions, 77 K, at which temperature it is possible to obtain well-resolved spectra. The measuring conditions of DR-UV-Vis spectra do not enable this resolution to be obtained.

For the undoped and Cd^{2+}-doped perovskite, a peak is observed at approximately 500 nm. As shown using XRD, these samples contain a small proportion of PbI_2. This emission at ~500 nm coincides with the band gap of the PbI_2, used as the reactant, and which was calculated using the Kubelka-Munk equation and Tauc law, obtaining a value of 2.35 eV. Figure S7 in the ESI shows the diffuse reflectance spectrum of the PbI_2 used.

2.6. Structure and local geometry analysis

First-principles calculations have shown to be an interesting tool in the theoretical study of doped perovskites.[26-29] So, based on the results of the experimental characterization, we performed theoretical calculations to gain a deeper understanding of the effect of metal doping on the structural and electronic properties of $MAPbI_3$ perovskites. A study was performed of the tetragonal structures of $MAPb_{1-x}B_xI_3$ with B= Sn^{2+}, Cd^{2+} and Sr^{2+}, and the cubic structure for $MAPb_{1-x}Ca_xI_3$, with x=0.10 in all cases. These structures are concordant with those obtained experimentally, as reported above.

The local geometry for the first coordination shell around the dopant for the most stable configuration of the optimized doped perovskite structures is shown in Figure 6. For the purpose of comparison, the figures also include the $MAPbI_3$ structure in both tetragonal

and cubic phases. Doping with Sn^{2+} and Sr^{2+} hardly produced structural changes in their local geometry, compared with the undoped structure. The most striking changes are produced with doping with Cd^{2+} and Ca^{2+}. The inclusion of both ions as dopants caused a distortion in the structure. In both cases the dopant-I distance decreased, more noticeably for the Cd (*c.a.* 4%) than for the Ca (*c.a.* 1%). These results suggest a strengthening of the interactions between Cd-I and Ca-I, as will be discussed below using the PDOS results. Looking at the ionic radii, the distortion of the structure after doping with Cd^{2+} and Ca^{2+} may be thought to be due exclusively to the smaller Cd^{2+} and Ca^{2+} ions. However, it is also necessary to consider electronic effects produced in structures doped with these elements, as the results from PDOS and ELF indicate, and which will be discussed below.

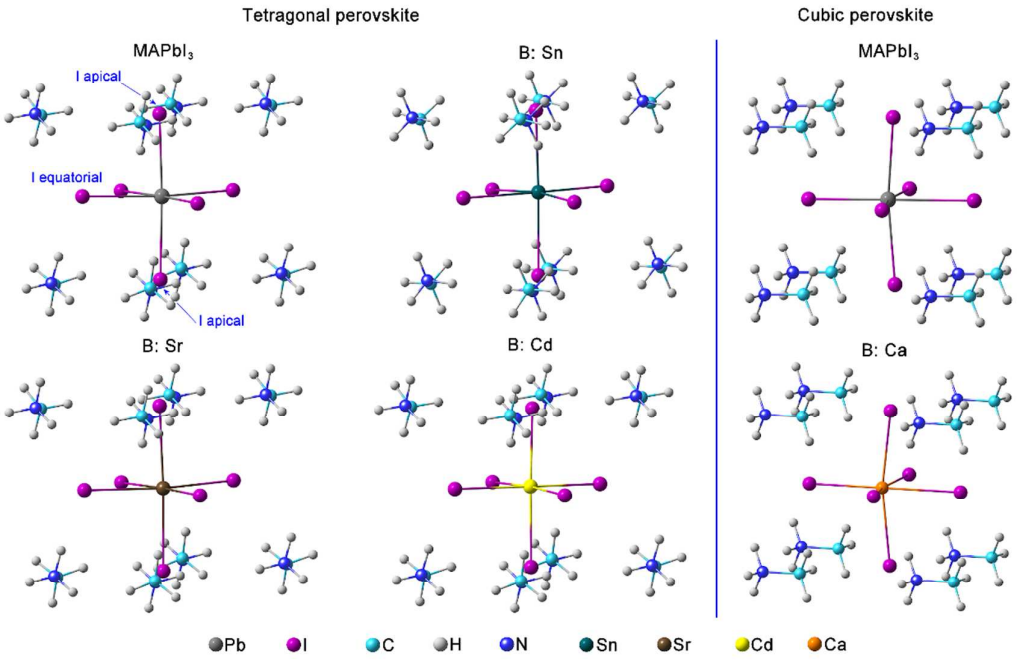

Figure 6. The local geometry of $MAPb_{1-x}B_xI_3$ around the dopant for the most stable configuration of undoped, Sn^{2+}-, Sr^{2+}- and Cd^{2+}-doped tetragonal perovskite, and undoped and Ca^{2+}-doped cubic perovskite.

2.7. DOS and PDOS analysis

The band gaps calculated by analysing the density of states (DOS) are in agreement with the experimental data. A slight decrease in the band gap values is observed for the different dopants, following the order Sn^{2+}>Cd^{2+}>Ca^{2+}>Sr^{2+} (see Figure 7).

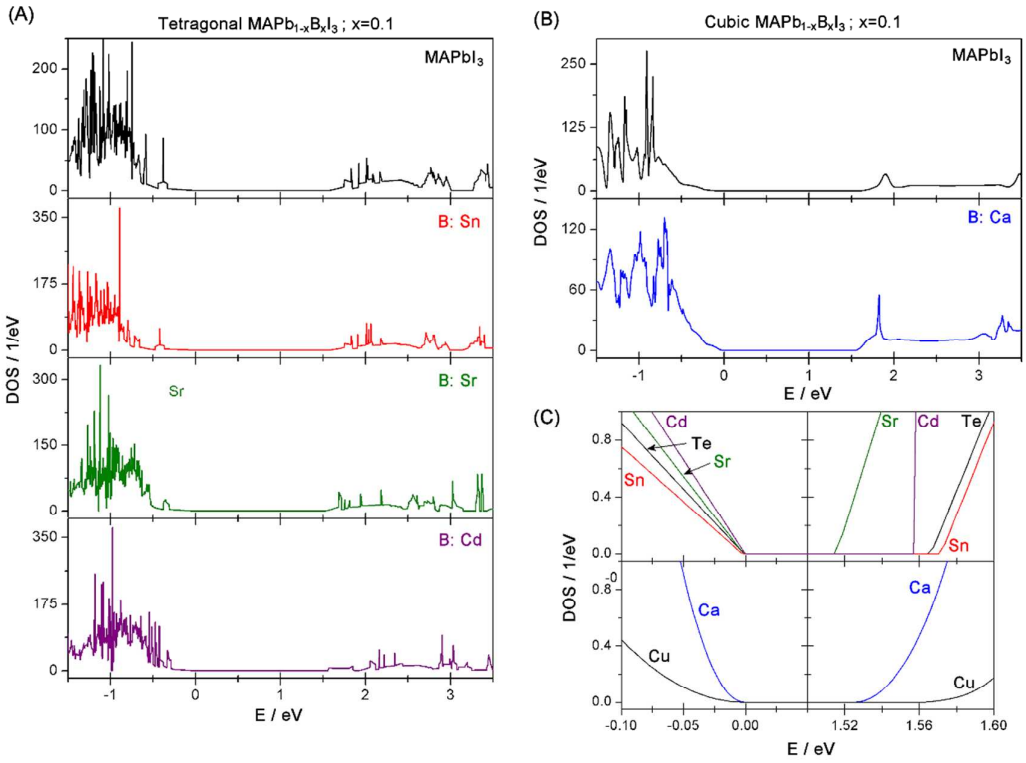

Figure 7. Total DOS plot for: (A) undoped and doped tetragonal, and (B) cubic $MAPbI_3$. (C) Representation of the VB and CB edges in all the cases.

The analysis of the projected density of states (PDOS) of the structures simulated indicates that, for the undoped optimized tetragonal and cubic structures, the valence band and conduction bands are mostly composed of I p and Pb p states, respectively, as reported elsewhere for both tetragonal and cubic phases.[8] Likewise, for all the doped structures, the valence band (VB) is mostly composed of I p states and the conduction band (CB) is dominated by the Pb p states, with a small contribution of B s, p and d states, where B=Sn, Sr, Cd, Ca, which varies depending on the dopant in each case.

Figure 8 shows the contribution of Pb and the dopants, I and MA groups to the VB and CB in all cases. Thus, it seems reasonable to consider that the decrease in the band gap is associated with the presence of the dopants, and in particular with the distribution of the s, p, and d states. However, it worth noting that in all cases there is a slight contribution of the s and p states of C and N, and s states of H belonging to the MA groups to both the VB and the CB, which are slightly modified in the doped samples, and so must also be connected with the lower band gap and must be taken into consideration. To clarify the role played by both the MA groups and each dopant in the decreased band gap, the description below will focus on discussing the interactions existing with the system formed by the MA groups located around the octahedron formed by six I atoms in the vertices around the central metal dopant (see Figure 6). To our knowledge, this is the first time a discussion of this kind has been performed.

Comparing the PDOS of the undoped and Sn-doped tetragonal phase structures, strong similarities can be found. Figures 8A and 8B show that a similar distribution of the states belonging to the elements C, N and H (total CHN states in Figure 8) and the s, p and d states of the six I atoms (total I states in Figure 8) for both structures. Likewise, Figure 8A and 8B show that the s states of Pb and Sn make the main contribution to the edge of the VB. Figure 9 shows in detail the contribution of the different states to the edge of the VB and CB in each case. However, the p states of Pb and Sn make the largest contribution to the edge of the CB with a minimal contribution from the d states (see Figure 9A and 9B). This explains why the band gap of the samples doped with Sn^{2+} are similar to the undoped samples, *c.a.* 1.57 eV, and why there is hardly any distortion in the structure due to the presence of Sn^{2+}, as stated above.

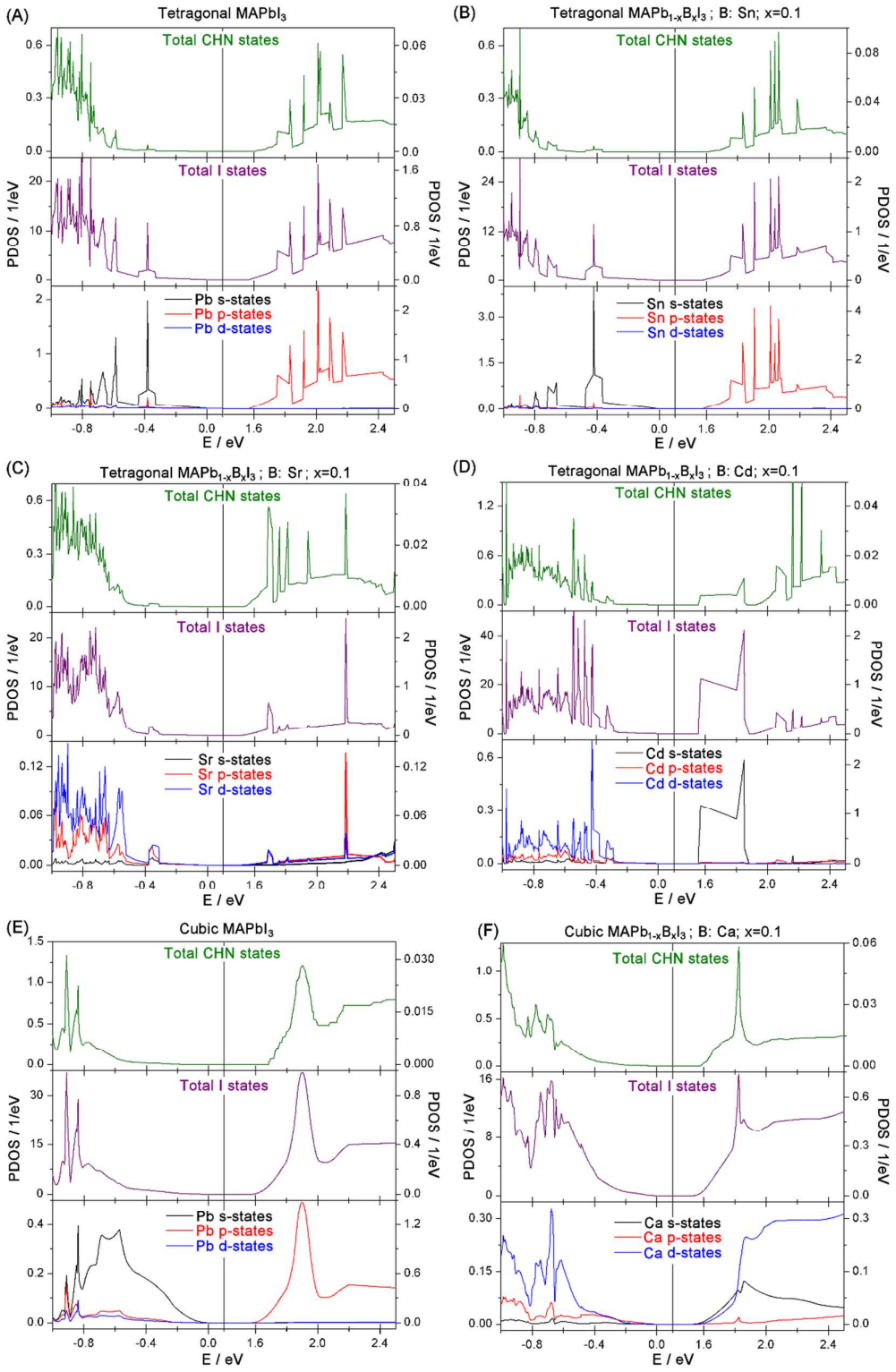

Figure 8. Total CHN, total I, Pb and B (=Sn, Sr, and Cd) projected states for tetragonal structures: (A)$MAPbI_3$; (B) $MAPb_{0.9}Sn_{0.1}I_3$; (C) $MAPb_{0.9}Sr_{0.1}I_3$; (D) $MAPb_{0.9}Cd_{0.1}I_3$; and cubic structures: (E) $MAPbI_3$; (F) $MAPb_{0.9}Ca_{0.1}I_3$.

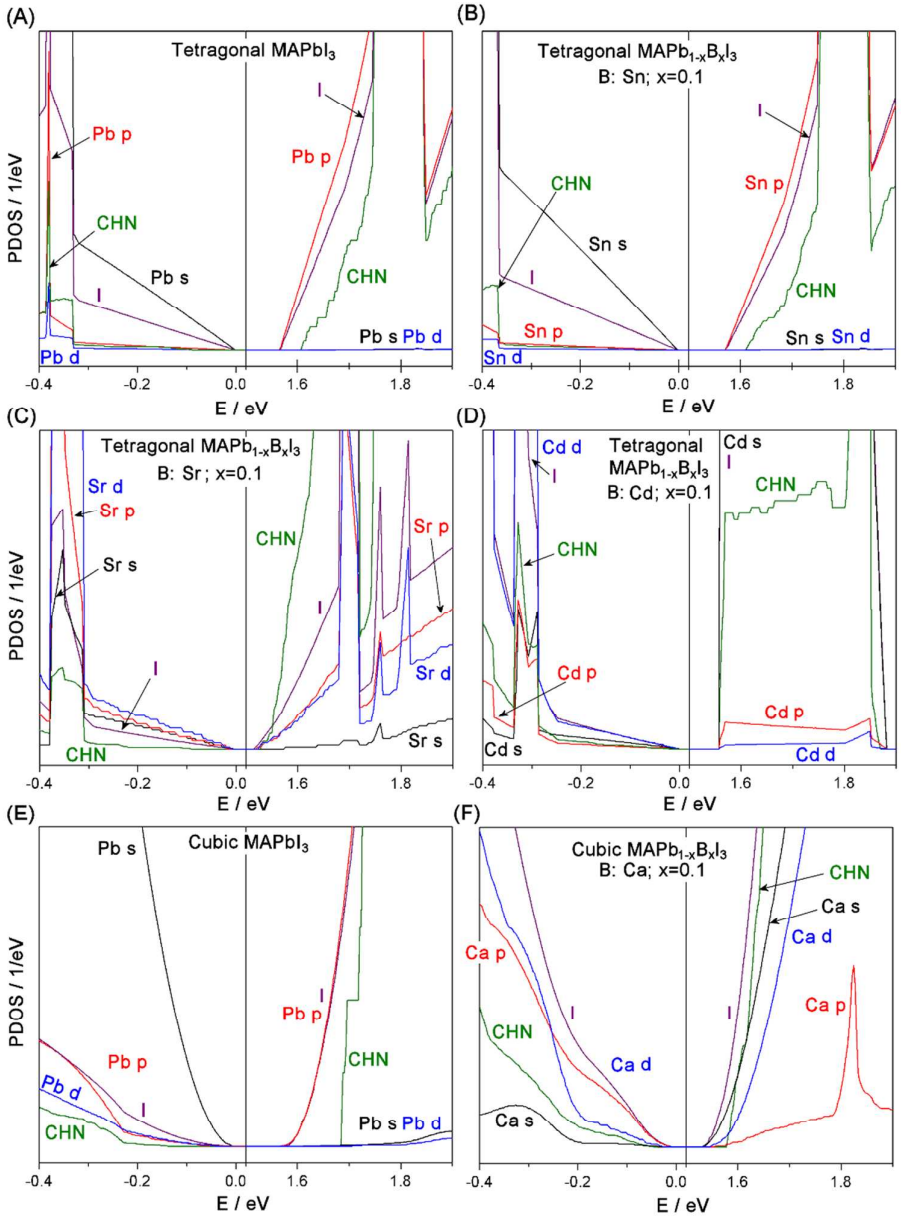

Figure 9. Detail of the contributions to the edges of VB and CB in all the cases.

Doping with Sr^{2+} produced the most significant decrease in the band gap, *c.a.* 1.50 eV, as reported above from the experimental results. Looking at the dopant, the contribution of the d- and p- states of Sr to the valence band was predominant (see Figure 8C), in particular the d-states that are near of the edge of the VB and they must play an important role in the charge transfer processes, as shown in Figure 9C. It is worth

mentioning that the contributions of Sr, I and the MA groups are much more displaced to the edges of the VB and the CB when compared with the undoped and Sn^{2+}-doped samples. Furthermore, the contribution of the CHN and I states stand out on the edge of CB (see Figure 9C). This result shows the important role played by I and the MA groups in the narrowing of the band gap. Figure 9C also shows the contribution of the d- and p-states of Sr to the edge of the CB, overlapping with the I and MA groups contributions. These interactions indicate that, although there are no structural distortions compared with the Sn^{2+}-doped and the undoped tetragonal structures, doping with Sr^{2+} led to electronic modifications that generated the narrowing of the band gap.

Figure 8D shows the PDOS for the Cd^{2+}-doped perovskite, whose band gap of *c.a.* 1.54 eV was in line with the experimental value. As with Sr, the predominant contribution to the edge of the VB is from the d and p states of the Cd (see Figure 9D). In this case, compared with the undoped and Sn^{2+}-doped structures, there is also a shift toward the edge of the VB and the CB of these Cd states, the C, H and N states of the MA groups, and the I states, but less than for Sr. As Figure 8D shows, there is a change in the shape of the CB in the case of Cd around 1.55 eV compared with the rest of the doped and undoped structures. At this level, the contribution of the Cd s states is predominant and there is overlapping with the states of I and the MA groups. As the atoms present suggest, a certain covalent contribution to the Cd-I bond is to be expected, as will be discussed below based on the results of the ELF.

Compared with the PDOS of the undoped structure with a cubic phase (Figure 8E) the VB and CB resemble those of the undoped tetragonal phase. As with the undoped tetragonal phase, the s and p states of Pb contribute predominantly to the VB and CB, respectively. However, when doped with Ca^{2+}, the d and p states make the biggest contribution to the VB, as occurred with doping with Cd^{2+} and Sr^{2+}. Furthermore, as in

these cases, they also overlap with the contributions of the I and the MA groups. Although the contribution of the d states of Ca to the edge of the CB is greater than that of Cd, the s states of the Ca also make a significant contribution to the edge of the CB (see Figure 9F). However, as with Sr, the contribution of the states of the I and the MA groups stands out on the edge of the CB. Once again, this result shows the important role played by the I and the MA groups in the narrowing of the band gap. Curiously, the direct band gap measured, *c.a.* 1.52 eV, although slightly bigger, resembles that of the Sr. In turn, for doping with Ca^{2+}, the electronic situation for the dopant-I and dopant-MA interactions is different (Figures 8E y 8F) to that of the undoped structure. This is due to the variation in the local environment caused by doping, which helps to explain the structural distortions mentioned above.

2.8. Electron Localization Function Study

The electronic properties of the different kinds of doping may be rationalized by means of the ELF study. Figure 10 shows the ELF containing the I atoms of the octahedron shown in Figure 6 in equatorial (down) and apical (up) positions, respectively. For comparative purposes, Figure 6 shows the apical and equatorial I atoms. So, Figures 10A and 10B show ELF plots for the tetragonal phase structure of the undoped and Sn-doped perovskite. These images are similar, which explains why there is no variation in their geometry. The PDOS analysis led to the same conclusion. On the other hand, doping with Sr^{2+} produced few geometrical changes, but there were electronic changes. Figure 10C shows how the contour plot for Sr is different to that of Pb and Sn, showing the more ionic nature of the Sr-I interaction. In fact, this more ionic nature is responsible for a slight increase in the negative charge, which is shared among the I atoms. There is also deformation of the contour of the apical and equatorial I atoms, that

can be seen in the apical plane (see enlarged Figure 10C, marked as 2) as a slight electronic localization (sky blue colour). For comparative purposes, an enlarged equivalent area of the undoped structure is shown (see Figure 10A), and Figure S8 shows the equivalent area for all the structures. Thus, this redistribution of electronic localization among the I atoms in the Sr-I interaction, together with the ionic radius of Sr^{2+}, similar to those of Sn^{2+} and Pb^{2+}, explains why there is no geometrical modification with regard to the undoped and Sn-doped structures.

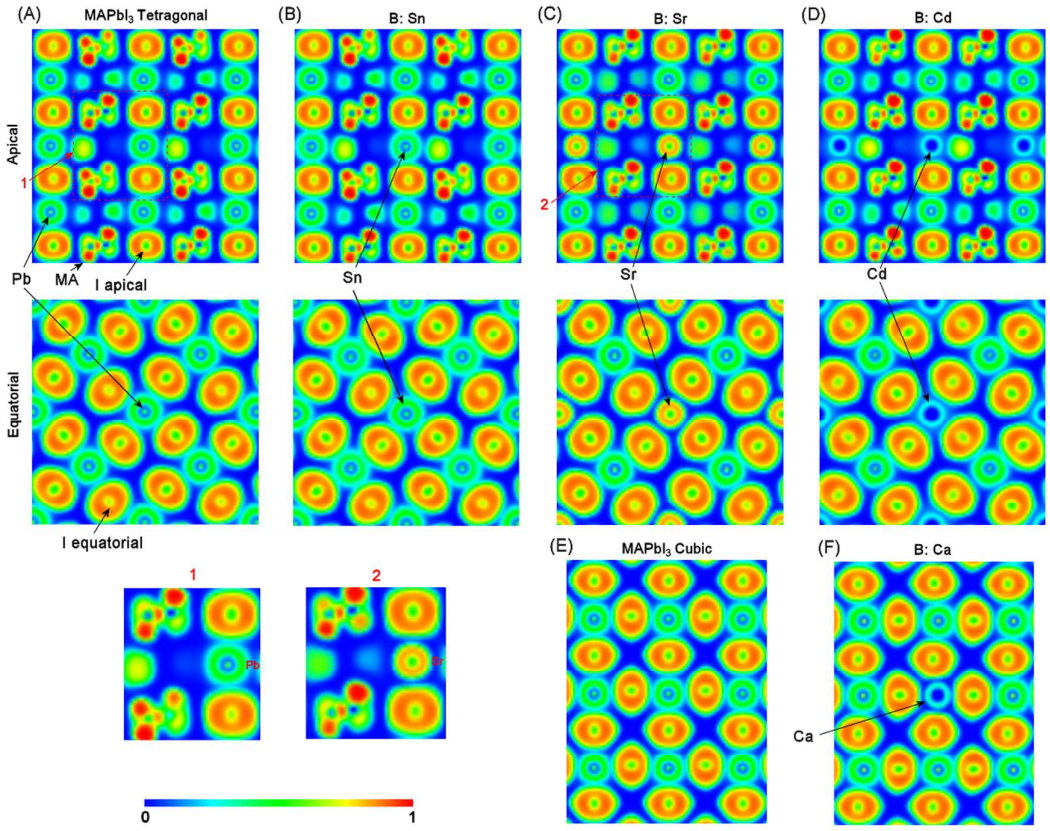

Figure 10. ELF contour plots for tetragonal structures: (A)$MAPbI_3$; (B) $MAPb_{0.9}Sn_{0.1}I_3$; (C) $MAPb_{0.9}Sr_{0.1}I_3$; (D) $MAPb_{0.9}Cd_{0.1}I_3$; and cubic structures: (E) $MAPbI_3$; (F) $MAPb_{0.9}Ca_{0.1}I_3$.

As Figure 10D shows, the situation with Cd^{2+} doping is different. It shows how the electron localization on Cd is lower than on Sr, which implies that the Cd-I interaction

is stronger than Sr-I, which coincides with the DOS analysis. Figure 10D down shows the interaction with Cd-I in the equatorial region. It shows that the ELF at the Cd-I site is polarized towards the Cd atoms, indicating directional bonding between the Cd and I atoms, which explains the geometric changes in the Cd-doped structures and that the Cd-I distances decrease by 4% compared with the undoped structure. In turn, Figures 10E and 10F compare the ELF of the undoped and Ca^{2+}-doped cubic phase structures. The ELF of the cubic phase is similar to that of the tetragonal phase. The electronic localization in the Ca is low and resembles that of the Cd doping, but unlike with Cd, there is no polarization in the interaction with the I atoms, so the Ca-I interaction is weaker than the Cd-I one. Thus, the Ca-I interaction has a more ionic nature than Cd-I even though Cd^{2+} and Ca^{2+} have similar ionic radii and low electronic localization. This explains why the Ca-I distances decreased by 1% compared with the undoped cubic phase structure.

2.9. Non-Covalent Interactions

An analysis tool to complement ELF consists of the study of weak interactions using the non-covalent interaction (NCI) index.[21] This index is based on electron density and its reduced gradient and enables the qualitative identification and characterisation of weak interactions of various strengths as chemically intuitive isosurfaces that reveal both stabilizing (strong and attractive interactions in blue, weak interactions in green) and destabilizing interactions (strong and repulsive interactions in red). Above, evidence has been given of how the slight contributions and overlaps in the same energy region of the DOS of the states of the MA groups with those of the Pb, the dopant B (B=Sn^{2+}, Sr^{2+}, Cd^{2+} and Ca^{2+}) or the nearby I atoms, are enough to affect the band gap. Thus, although these interactions in this kind of hybrid systems are weak, they are possible to detect by

means of NCI analysis, something that has not been performed before in this kind of systems.

Figure 11 shows a cut from the apical zone of the octahedron formed by the I atoms around the metal including the MA groups for the structures in undoped and Sn^{2+}-, Sr^{2+}-, and Cd^{2+}-doped tetragonal phase. Most striking at first is the role played by weak interactions (green colour) in stabilizing the structure, where the MA groups play an essential role. For dopant-MA interactions, curiously, this kind of weak-type stabilizing interactions is stronger in the Sr^{2+}-doped structure, above all in the region between two equatorial I atoms (marked as 1 in Figure 11). This is in agreement with the results from ELF, which showed an increase in electron localization in this region.

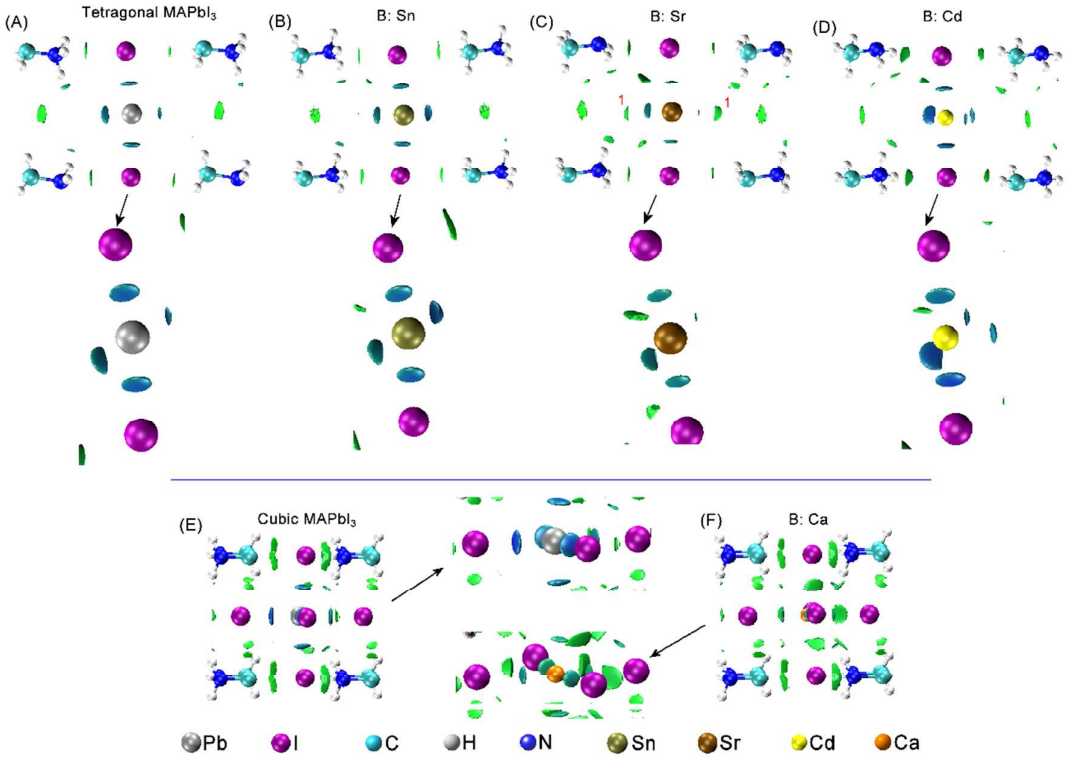

Figure 11. NCI plots for tetragonal structures: (A)$MAPbI_3$; (B) $MAPb_{0.9}Sn_{0.1}I_3$; (C) $MAPb_{0.9}Sr_{0.1}I_3$; (D) $MAPb_{0.9}Cd_{0.1}I_3$; and cubic structures: (E) $MAPbI_3$; (F) $MAPb_{0.9}Ca_{0.1}I_3$.

On the other hand, looking at the dopant-I interaction in the enlarged area of Figure 11, there are different tones of colour indicating the strength of the interactions, which follow the order Cd-I>Sn-I≈Pb-I>Sr-I. In this case, the strongest blue colour is for doping with Cd^{2+}, indicating that this is the strongest interaction. This is followed by the undoped structure and the Sn^{2+}-doped one, which have a similar light blue colour. Finally, the weakest interaction corresponds to doping with Sr^{2+}, which has a greenish blue colour.

Comparing the NCI plot of the undoped and Ca^{2+}-doped cubic phase (Figure 11E and 11F), it is possible to see that the Ca-I interaction is weaker, having a greenish blue colour compared with the blue of the Pb-I interaction of the undoped structure. Nevertheless, the smaller size of the Ca^{2+} leads to a reorganisation of the structure and an increase in stabilizing interactions (green colour), which the ELF plots also suggest.

3. Experimental and Computational section

3.1. Experimental

The synthesis of $MAPb_{1-x}B_xI_3$ species (where MA=CH_3NH_3; and B=Sn^{2+}, Sr^{2+}, Cd^{2+}, Ca^{2+}) was performed by first synthesizing CH_3NH_3I.[12, 30, 31] Then, the reaction was performed with PbI_2 and BI_2, using the stoichiometric quantities necessary to obtain x values of 0.05, 0.10 and 0.15. The methodology followed is detailed below.

Synthesis of CH_3NH_3I. Methylamine (CH_3NH_2, 11.33 mL, 0.091 mol, 33 wt.% in ethanol, Sigma Aldrich) and hydroiodic acid (HI, 10 mL, 0.076 mol, 57 wt.% in water, Aldrich) were stirred in an ice bath for 2 hours controlling the temperature continuously. Then, the solution was evaporated at 50 ºC for 1 h, and CH_3NH_3I was

obtained. Finally, the solid obtained was washed three times with diethyl ether (purity ≥ 99.8%, Sigma Aldrich) and dried at 50ºC on a hot plate.

Synthesis of $CH_3NH_3PbI_3$. The synthesized CH_3NH_3I (0.395 g) and PbI_2 (1.157 g, purity 99%, Sigma Aldrich) were mixed in γ-butyrolactone (2 mL, purity ≥ 99%, Sigma Aldrich,) at 60 ºC for 18 h.

Synthesis of $CH_3NH_3Pb_{1-x}B_xI_3$. For the doped samples, the same amount of synthesized CH_3NH_3I was used as in the previous case and the required stoichiometric amounts of PbI_2 and BI_2 were introduced to obtain the values, x = 0.05, 0.10 and 0.15 (SnI_2, purity 99.999%; SrI_2, purity > 99.99%; CdI_2, purity 99.999%; CaI_2, purity 99%; supplied by Sigma Aldrich). Therefore, the synthesized CH_3NH_3I (0.395 g), PbI_2 (the amount corresponding to the 1-x value) and BI_2 (being B: Sn, Sr, Cd, Ca; adding the amount corresponding to the x value) were mixed in γ-butyrolactone (2 mL, purity ≥ 99%, Sigma Aldrich,) at 60 ºC for 18 h.

Characterization. The elemental analysis was performed using two instrumental techniques. The CHNS technique was used to determine the amount of C, N and H, using an elemental analyser supplied by Leco©, model CHNS932. Next, X-ray fluorescence was performed to determine the amount of Pb, I and the B dopant (=Sn^{2+}, Sr^{2+}, Cd^{2+}, Ca^{2+}), using a sequential XRF spectrometer supplied by Bruker©, model Pioneer S4.

In addition, X-ray diffraction (XRD) was used to determine the crystalline phases in the samples. A diffractometer supplied by Bruker©, model D8 Discover, with Cu-Kα radiation was used to register the patterns. The scan conditions were from 20 to 70º in

2θ with a resolution of 0.02º, 40 kV and 40 mA. In addition, optical band gap values (E_g) were determined from diffuse reflectance measurements. The equipment, assembled in our laboratory, was composed of a Xenon lamp, model ASB-XE-175, supplied by Spectral Products©, as the illumination source; a USB2000+ spectrometer supplied by Ocean Optics©; and an integrating sphere from Spectra Tech©. In turn, X-ray photoelectron spectroscopy (XPS) was used to analyse the chemical bonding states and the chemical composition of the samples. The XPS spectra were registered using a Kratos Axis UltraDLD spectrometer, with monochromatized Al Kα radiation (1486.6 eV), a 20 eV pass energy and given with an accuracy of 0.1 eV. Samples were pressed into self-supported wafers and analysed without any further treatment. Electrostatic charging effects could be stabilized with the help of the specific device developed by Kratos.

Finally, Cathodoluminescence (CL) measurements were performed to study the emission of the samples. All the CL experiments were performed using a CL setup developed in our own laboratory based on a FEI thermal field emission SEM/Sirion, reaching a nominal spatial resolution of 25 nm. The luminescence of the sample is collected from the irradiated area and spectrally diffracted in a Jobin Yvon© HR320 spectrometer system (EM-CCD 1200×256 pixels coupled with a 320 mm focal length spectrometer). The measurements were performed at about 77 K with an electron beam energy of 10 keV.

3.2. Computational framework

DFT-periodic calculations were performed using the Vienna Ab Initio Simulation Package (VASP)[32-35] with the projector-augmented wave (PAW) method.[36, 37] The number of plane waves in VASP was controlled by a cut-off energy, set in our

calculations to E_{cut}=500 eV to satisfactorily describe the system.[38] The electron exchange and correlation were treated within the generalized gradient approximation (GGA).[39] In the case of GGA, Perdew-Burke-Ernzerhof (PBE)[39] functionals were used. Both the cell shape and atomic positions were optimized using a conjugate-gradient algorithm, where the iterative relaxation of atomic positions was stopped when the forces on the atoms were less than 0.01 eV/Å. Also, a Gaussian smearing with k_BT=0.1365 eV was applied.

Perovskite tetragonal and cubic phases were characterized by the I4/mcm and Pm3m space groups, respectively.[8] The tag KSPACING determined the number of k-points in the mesh. A value of 0.4 for sampling the Brillouin zone for perovskite bulk was enough to obtain negligible changes in the optimized cell parameters and energy. The resulting cell parameters were a = 8.912 Å, c = 12.707 Å and a = 6.299 Å for the tetragonal and cubic phases, respectively, in agreement with the experimental values (a = 8.874 Å, c = 12.671 Å and a = 6.276 Å).[8]

The $(MA)_8Pb_8I_{24}$ cell was optimized as a model for the tetragonal and cubic phases of perovskite models to simulate doping of 10%. The incorporation of each dopant (Sn, Sr, Cd and Ca) into the structure was performed in substitutional positions. The dopant atom substitutes the Pb atom in the perovskite structure taking into account the equivalent sites. A study was performed of the tetragonal structures of $MAPb_{1-x}B_xI_3$ with B= Sn, Cd and Sr, and the cubic structure for $MAPb_{1-x}Ca_xI_3$, with x=0.10 in all cases. The structures $(MA)_8Pb_7SnI_{24}$, $(MA)_8Pb_7SrI_{24}$, $(MA)_8Pb_7CdI_{24}$ and $(MA)_8Pb_7CaI_{24}$ were optimized to simulate the experimental stoichiometries in the doping range. The selected structures were adequate to represent qualitatively the experimental concentrations within DFT with a periodic boundary condition framework.

Close attention was paid to the orientational disorder of MA within the tetragonal structure, reporting the most stable configuration for each doped structure. Thus, different conformations were optimized based on the orientations of the four organic molecules, whose starting configurations are included in the ESI (Figure S9). For comparison purposes, for the cubic phase, the MA arrangement chosen was the most stable configuration of the tetragonal phase.

The density of states (DOS) and projected density of states (PDOS) for the relaxed structures were obtained using the tetrahedron method with Blöchl corrections[40] and a KSPACING of 0.3. For all the systems, DFT+U[41] calculations were performed to take into account the on-site Coulomb interaction; thus, we have used a U value of 5 eV for d orbitals, and -3.5 eV for p orbitals of Ca and Sr (SIC method).[42]

Electron localization function (ELF)[16-20] images and structure images were obtained using the Vaspview software[43] and ChemCraft 1.6,[44] respectively. The non-covalent interaction analysis was performed with CRITIC2 software.[45, 46] NCI images were made with VMD software.[47] VMD is developed with NIH support by the Theoretical and Computational Biophysics group at the Beckman Institute, University of Illinois at Urbana-Champaign.

4. Conclusions

This paper presents the synthesis of organic-inorganic hybrid perovskite $CH_3NH_3PbI_3$ doped with Sn^{2+}, Sr^{2+}, Cd^{2+} and Ca^{2+} in the position of the Pb^{2+} ion. The kind of dopants affected both the crystalline phase and the band gap energy. Undoped perovskite has a tetragonal crystalline structure (I4/mcm space group), which was maintained with all the dopants used, except Ca^{2+}, in which case a cubic phase (Pm3m space group) was obtained as the predominant crystalline phase. The band gap of the samples was also

affected by doping. In the case of the tetragonal structures, after Sn^{2+} doping, the band gap remained similar to that of the undoped perovskite, but decreased slightly with Sr^{2+} and Cd^{2+} doping. The largest decrease, of up to 4.5%, was seen with doping with Sr^{2+}. As for the cubic structure, the band gap of the Ca^{2+}-doped samples decreased compared with the values reported for cubic phase. The band gap values obtained experimentally were concordant with those reached using theoretical calculations. DFT calculations showed band gap narrowing between the valence-band-maximum (VBM) and the conduction-band minimum (CBM), in line with the values obtained experimentally. Both results suggest that the greater the ionic nature of the interaction between the metal dopant and I, the lower the band gap, which was the case of Sr^{2+} for the tetragonal phase and Ca^{2+} for the cubic phase. Furthermore, the NCI analysis complemented the results from ELF and indicated that the strength of the dopant-I interaction follows the order Cd-I>Sn-I≈Pb-I>Sr-I for the tetragonal structure. Likewise, in the case of the cubic structure, after doping with Ca^{2+} the Ca-I interaction shows a greater ionic nature than Cd-I even though Cd^{2+} and Ca^{2+} have similar ionic radii and low electronic localization, as ELF shows. Finally, the NCI analysis also showed the importance of weak interactions in stabilizing these hybrid structures, in which the MA groups play an essential role.

Acknowledgements
We thank the Junta de Andalucía of Spain under projects P09-FQM-04938, and FEDER funds. Calculations were done through CICA - Centro Informático Científico de Andalucía (Spain).

Electronic Supplementary Information (ESI) available: Analysis elemental obtained by ICP-AES, and XRF (Table S1). XRD patterns of the samples synthesized (Figure S1). XRD patterns of commercials PbI_2 and CdI_2 used as reagents (Figure S2). XRD patterns of $MAPb_{0.5}Sn_{0.5}I_3$ (Figure S3). UV-Vis spectra, in mode reflectance diffuse, of

the samples synthesized (Figure S4). UV-Vis spectra, in mode reflectance diffuse, of $MAPbI_3$ and $MAPb_{0.5}Sn_{0.5}I_3$ samples (Figure S5). XPS spectra for $MAPbI_3$; and $MAPb_{1-x}B_xI_3$ (B: Sn, Sr, Cd, Ca) with x=0.10 (Figure S6). UV-Vis spectra, in mode reflectance diffuse, of commercial PbI_2 used as a reagent (Figure S7). Detail of the ELF for the simulated structures (Figure S8). Starting configurations of the MA groups in the structure (Figure S9). See DOI: 10.1039/b000000x/.

References

1. Y. Y. Li, G. L. Zheng, C. K. Lin and J. Lin, *Cryst Growth Des*, 2008, **8**, 1990-1996.
2. P. J. Baker, T. Lancaster, I. Franke, W. Hayes, S. J. Blundell, F. L. Pratt, P. Jain, Z. M. Wang and M. Kurmoo, *Phys Rev B*, 2010, **82**.
3. C. R. Kagan, D. B. Mitzi and C. D. Dimitrakopoulos, *Science*, 1999, **286**, 945-947.
4. M. M. Lee, J. Teuscher, T. Miyasaka, T. N. Murakami and H. J. Snaith, *Science*, 2012, **338**, 643-647.
5. Y. Ogomi, A. Morita, S. Tsukamoto, T. Saitho, N. Fujikawa, Q. Shen, T. Toyoda, K. Yoshino, S. S. Pandey, T. L. Ma and S. Hayase, *J Phys Chem Lett*, 2014, **5**, 1004-1011.
6. F. Hao, C. C. Stoumpos, R. P. H. Chang and M. G. Kanatzidis, *J Am Chem Soc*, 2014, **136**, 8094-8099.
7. E. Mosconi, A. Amat, M. K. Nazeeruddin, M. Gratzel and F. De Angelis, *J Phys Chem C*, 2013, **117**, 13902-13913.
8. T. Baikie, Y. N. Fang, J. M. Kadro, M. Schreyer, F. X. Wei, S. G. Mhaisalkar, M. Graetzel and T. J. White, *J Mater Chem A*, 2013, **1**, 5628-5641.
9. M. Z. Liu, M. B. Johnston and H. J. Snaith, *Nature*, 2013, **501**, 395-+.
10. J. H. Noh, S. H. Im, J. H. Heo, T. N. Mandal and S. I. Seok, *Nano Lett*, 2013, **13**, 1764-1769.
11. J. Burschka, N. Pellet, S. J. Moon, R. Humphry-Baker, P. Gao, M. K. Nazeeruddin and M. Gratzel, *Nature*, 2013, **499**, 316-+.
12. H. S. Kim, C. R. Lee, J. H. Im, K. B. Lee, T. Moehl, A. Marchioro, S. J. Moon, R. Humphry-Baker, J. H. Yum, J. E. Moser, M. Gratzel and N. G. Park, *Sci Rep-Uk*, 2012, **2**.
13. J. M. Ball, M. M. Lee, A. Hey and H. J. Snaith, *Energ Environ Sci*, 2013, **6**, 1739-1743.
14. M. Graetzel, R. A. J. Janssen, D. B. Mitzi and E. H. Sargent, *Nature*, 2012, **488**, 304-312.
15. P. Umari, E. Mosconi and F. De Angelis, *Sci Rep-Uk*, 2014, **4**.
16. A. D. Becke and K. E. Edgecombe, *J Chem Phys*, 1990, **92**, 5397-5403.
17. B. Silvi and A. Savin, *Nature*, 1994, **371**, 683-686.
18. B. Silvi and C. Gatti, *J Phys Chem A*, 2000, **104**, 947-953.
19. A. Savin, A. D. Becke, J. Flad, R. Nesper, H. Preuss and H. G. Vonschnering, *Angew Chem Int Edit*, 1991, **30**, 409-412.
20. A. Savin, O. Jepsen, J. Flad, O. K. Andersen, H. Preuss and H. G. Vonschnering, *Angew Chem Int Edit*, 1992, **31**, 187-188.
21. E. R. Johnson, S. Keinan, P. Mori-Sanchez, J. Contreras-Garcia, A. J. Cohen and W. T. Yang, *J Am Chem Soc*, 2010, **132**, 6498-6506.
22. A. Poglitsch and D. Weber, *J Chem Phys*, 1987, **87**, 6373-6378.
23. A. Kojima, K. Teshima, Y. Shirai and T. Miyasaka, *J Am Chem Soc*, 2009, **131**, 6050-+.
24. L. F. Gate, *Appl Optics*, 1974, **13**, 236-238.
25. A. K.-V. A. V. G. Naumkin, S. W.; C. J. Powell, *in NIST Standard Reference Database 20, Version 4.1, Gaithersburg*, 2012.
26. Y. Takahashi, R. Obara, Z. Z. Lin, Y. Takahashi, T. Naito, T. Inabe, S. Ishibashi and K. Terakura, *Dalton T*, 2011, **40**, 5563-5568.

27. G. Giorgi, J. I. Fujisawa, H. Segawa and K. Yamashita, *J Phys Chem C*, 2014, **118**, 12176-12183.
28. T. Umebayashi, K. Asai, T. Kondo and A. Nakao, *Phys Rev B*, 2003, **67**.
29. F. Brivio, A. B. Walker and A. Walsh, *Apl Mater*, 2013, **1**.
30. S. R. Jang, K. Zhu, M. J. Ko, K. Kim, C. Kim, N. G. Park and A. J. Frank, *Acs Nano*, 2011, **5**, 8267-8274.
31. Z. L. Chen, H.; Tang, Y.; Huang, X.; Ho, D.; Lee, C.-S., *Materials Research Express*, 2014, **1**, 015034.
32. G. Kresse and J. Hafner, *Phys Rev B*, 1993, **47**, 558-561.
33. G. Kresse and J. Hafner, *Phys Rev B*, 1994, **49**, 14251-14269.
34. G. Kresse and J. Furthmuller, *Comp Mater Sci*, 1996, **6**, 15-50.
35. G. Kresse and J. Furthmuller, *Phys Rev B*, 1996, **54**, 11169-11186.
36. P. E. Blochl, *Phys Rev B*, 1994, **50**, 17953-17979.
37. G. Kresse and D. Joubert, *Phys Rev B*, 1999, **59**, 1758-1775.
38. Y. Ortega, N. C. Hernandez, E. Menendez-Proupin, J. Graciani and J. F. Sanz, *Phys Chem Chem Phys*, 2011, **13**, 11340-11350.
39. J. P. Perdew, K. Burke and M. Ernzerhof, *Physical Review Letters*, 1996, **77**, 3865-3868.
40. P. E. Blochl, O. Jepsen and O. K. Andersen, *Phys Rev B*, 1994, **49**, 16223-16233.
41. S. L. Dudarev, G. A. Botton, S. Y. Savrasov, C. J. Humphreys and A. P. Sutton, *Phys Rev B*, 1998, **57**, 1505-1509.
42. E. Menendez-Proupin, A. Amezaga and N. C. Hernandez, *Physica B*, 2014, **452**, 119-123.
43. T. B. Terriberry, D. F. Cox and D. A. Bowman, *Comput Chem*, 2002, **26**, 313-319.
44. www.chemcraftprog.com.
45. A. Otero-de-la-Roza, E. R. Johnson and V. Luana, *Comput Phys Commun*, 2014, **185**, 1007-1018.
46. A. Otero-de-la-Roza, M. A. Blanco, A. M. Pendas and V. Luana, *Comput Phys Commun*, 2009, **180**, 157-166.
47. W. Humphrey, A. Dalke and K. Schulten, *J Mol Graph Model*, 1996, **14**, 33-38.